A RESTART PROCEDURE FOR THE FINITE MASS METHOD *

MARKUS KLINGLER, PETER LEINEN, † AND HARRY YSERENTANT ‡

Abstract. The finite mass method is a gridless Lagrangian method to simulate compressible flows that has been developed by Gauger, Leinen, and Yserentant [*SIAM J. Numer. Anal.,* 37 (2000), pp. 1768–1799]. It is based on a discretization of mass, not of space as with classical discretization schemes. Mass is subdivided into little mass packets of finite extension each of which is equipped with finitely many internal degrees of freedom. These mass packets move under the influence of internal and external forces and the laws of thermodynamics and can change their size, orientation, and shape to follow the motion of the fluid. The ability of the mass packets to deform with the flow is the reason for the high accuracy of the finite mass method, but also requires that the computation is newly set up from time to time. Such restart procedures are described in this article.

Key words. finite mass method, gridless discretizations, compressible fluids

AMS subject classifications. 76N99, 76M25, 65M99

DOI. will hopefully sometime exist

1. Introduction. The finite mass method was introduced in [4] and [8] and is founded on concepts developed in [13], [14] and [15]. It is a gridless Lagrangian method to solve problems in fluid mechanics and is based, in contrast to standard methods, on a discretization of mass, not of space. Mass is subdivided into small mass packets that move independently of each other under the influence of internal and external forces and the laws of thermodynamics and normally overlap. The approximations the finite mass method delivers are smooth functions and not discrete measures, so that it comes closer to classical discretizations than to usual particle methods.

The high accuracy of the finite mass method origins from the ability of the mass packets to rotate, to expand, to contract, and to deform with the flow, but this ability also leads to problems when particles degenerate or do not any longer align sufficiently well with each other. In such situations, the computation must be newly set up and the mass density, the velocity field, and the other field quantities must be represented by a new set of non-deformed particles again aligned with an appropriate grid. At first sight, this reminds of Godunov-type methods [9], [10], for example, in which the information is remapped after every timestep to the given grid. But in comparison with such grid-oriented methods, recovery steps of this kind are only very seldom necessary in the finite mass method, typically after certain fixed time intervals, and not after every timestep. Therefore much less diffusion is introduced and the method keeps its favorable properties as an essentially gridless Lagrangian method.

The restart procedure developed in this article is of purely local nature and maintains the formal order accuracy of the finite mass method. It is itself gridless as it concerns the transfer of the velocity field to the new particles. Quantities like the mass density are transferred by a quasi-interpolation method to the new representation. More involved total variation diminishing schemes related to those [1], [12] used in image processing are not treated in this paper. For the application of such techniques to the finite mass method, we refer to the thesis of Gauger [3].

* Received by the editors February 29, 2004 (not really, took much longer), accepted for publication February 29, 2008 (if ever), published electronically December 24, 2012 (maybe), http://siam.org/journals/sisc/100-1/111111.html

† Rechenzentrum, Universität Trier, 54286 Trier, Germany (leinen@uni-trier.de)

‡ Institut für Mathematik, TU Berlin, 10623 Berlin, Germany (yserentant@math.tu-berlin.de)

2. A short review of the finite mass method. The basic ingredient of the finite mass method is an at least continuously differentiable shape function $\psi\colon\mathbb{R}^d \to \mathbb{R}$, d the space dimension, having a compact support and attaining only values ≥ 0. It describes the mass distribution inside the mass packets into which the fluid is subdivided. Without restriction, the normalization conditions

$$\int \psi(\mathbf{y})\,\mathrm{d}\mathbf{y} = 1, \quad \int \psi(\mathbf{y})\mathbf{y}\,\mathrm{d}\mathbf{y} = \mathbf{0} \tag{2.1}$$

fixing the mass of the reference particle and the position of its barycenter and

$$\int \psi(\mathbf{y})\, y_k y_l\,\mathrm{d}\mathbf{y} \;=\; J\,\delta_{kl} \tag{2.2}$$

to its inertia tensor are assumed, where the y_k denote the components of $\mathbf{y}$. The shape function ψ may, for example, be the tensor product

$$\psi(\mathbf{y}) = \prod_{k=1}^{d} \widetilde{\psi}(y_k) \tag{2.3}$$

of a function $\widetilde{\psi}$ in one space variable. A suitable $\widetilde{\psi}$, which we have used in the numerical experiments in section 5, is the normalized third order B-spline given by

$$\widetilde{\psi}(\xi) = \frac{1}{6}\begin{cases} (2+\xi)^3, & -2 \leq \xi \leq -1, \\ 4 - 3\xi^2(2+\xi), & -1 \leq \xi \leq 0, \\ 4 - 3\xi^2(2-\xi), & 0 \leq \xi \leq 1, \\ (2-\xi)^3, & 1 \leq \xi \leq 2, \end{cases} \tag{2.4}$$

for $|\xi| \leq 2$ and by $\widetilde{\psi}(\xi) = 0$ for $|\xi| > 2$. It can be composed of smaller copies and be used to build up a basis for the cubic spline functions on a uniform grid. This $\widetilde{\psi}$ fulfills the conditions (2.1) and (2.2) where the constant J here takes the value

$$J = \frac{1}{3}. \tag{2.5}$$

The single mass packets or particles can move in space and can undergo arbitrary linear deformations. The points $\mathbf{y}$ of the mass packet i move along the trajectories

$$t \;\to\; \mathbf{q}_i(t) + \mathbf{H}_i(t)\mathbf{y}, \quad \det \mathbf{H}_i(t) > 0. \tag{2.6}$$

The vector $\mathbf{q}_i(t)$ determines the position of the packet and the matrix $\mathbf{H}_i(t)$ its size, shape and orientation in space. Conversely,

$$\mathbf{y} \;=\; \mathbf{H}_i(t)^{-1}(\mathbf{x} - \mathbf{q}_i(t)) \tag{2.7}$$

are the material or body coordinates of the point at position $\mathbf{x}$ in space at time t. The mass density of the packet i related to space coordinates therefore reads, up to its constant total mass m_i,

$$\psi_i(\mathbf{x}, t) \;=\; \frac{\psi\big(\mathbf{H}_i(t)^{-1}(\mathbf{x} - \mathbf{q}_i(t))\big)}{\det \mathbf{H}_i(t)}; \tag{2.8}$$

the determinant ensures that

$$\int \psi_i(\mathbf{x}, t)\,\mathrm{d}\mathbf{x} \;=\; 1 \tag{2.9}$$

independent of the position vector $\mathbf{q}_i$ and the deformation matrix $\mathbf{H}_i$ so that the total mass contained in this packet remains fixed. The total mass density

$$\rho(\mathbf{x},t) = \sum_{i=1}^{N} m_i \psi_i(\mathbf{x},t) \tag{2.10}$$

then results from the superposition of the mass densities of the single packets.

The point of the particle i with the material coordinates $\mathbf{y}$ has the velocity

$$t \;\rightarrow\; \mathbf{q}_i'(t) + \mathbf{H}_i'(t)\mathbf{y}. \tag{2.11}$$

Inserting the expression (2.7) for $\mathbf{y}$, one gets the velocity field

$$\mathbf{v}_i(\mathbf{x},t) = \mathbf{q}_i'(t) + \mathbf{H}_i'(t)\mathbf{H}_i(t)^{-1}(\mathbf{x}-\mathbf{q}_i(t)) \tag{2.12}$$

of the packet i related to the fixed space coordinates. The mass fluxes of the single packets superimpose to the total mass flux

$$(\rho\mathbf{v})(\mathbf{x},t) = \sum_{i=1}^{N} m_i \psi_i(\mathbf{x},t)\, \mathbf{v}_i(\mathbf{x},t) \tag{2.13}$$

implicitly defining the velocity field

$$\mathbf{v}(\mathbf{x},t) = \sum_{i=1}^{N} \chi_i(\mathbf{x},t)\mathbf{v}_i(\mathbf{x},t) \tag{2.14}$$

where the χ_i denote the local mass fractions

$$\chi_i(\mathbf{x},t) = \frac{m_i \psi_i(\mathbf{x},t)}{\rho(\mathbf{x},t)} \tag{2.15}$$

of the single packets. The χ_i form a partition of unity on the region actually occupied by mass so that the velocity field (2.14) is a convex combination of the velocity fields of the particles with nonzero mass densities at the given point in space.

The construction ensures conservation of mass as expressed by the relation

$$\frac{\partial \psi_i}{\partial t} + \operatorname{div}(\psi_i \mathbf{v}_i) = 0 \tag{2.16}$$

for the mass densities and velocity fields of the single particles. This conservation law immediately implies the continuity equation

$$\frac{\partial \rho}{\partial t} + \operatorname{div}(\rho\mathbf{v}) = 0 \tag{2.17}$$

for the mass density (2.10) and the velocity field (2.14) or the globally defined mass flux (2.13). Independent of the underlying dynamics, the mass density (2.10) and the velocity field (2.14) are compatible to each other and correctly describe a mass flow.

To get an impression of the attainable accuracy, we start from a given twice continuously differentiable velocity field $\mathbf{u}$. Then fixing the particle trajectories $\mathbf{q}_i$ and the matrices $\mathbf{H}_i$, with given initial values, as solutions of the differential equations

$$\mathbf{q}_i'(t) = \mathbf{u}(\mathbf{q}_i(t),t), \quad \mathbf{H}_i'(t) = (\nabla\mathbf{u})(\mathbf{q}_i(t),t)\,\mathbf{H}_i(t), \tag{2.18}$$

the velocity field (2.12) of the particle i reads

$$\mathbf{v}_i(\mathbf{x},t) = \mathbf{u}(\mathbf{q}_i(t),t) + (\nabla\mathbf{u})(\mathbf{q}_i(t),t)(\mathbf{x}-\mathbf{q}_i(t)) \tag{2.19}$$

and thus is a second order approximation of $\mathbf{u}$ in a neighborhood of $\mathbf{x} = \mathbf{q}_i(t)$. As the mass fractions (2.15) form a partition of unity, the resulting overall velocity field

$$\mathbf{v}(\mathbf{x},t) = \mathbf{u}(\mathbf{x},t) + \sum_{i=1}^{N} \chi_i(\mathbf{x},t)(\mathbf{v}_i-\mathbf{u})(\mathbf{x},t) \tag{2.20}$$

remains a second order approximation of $\mathbf{u}$ on the region occupied by mass, independent of where the particles are located and how they are deformed. The mass density is an exact solution of the transport equation (2.17) with respect to this perturbed velocity field and therefore, with corresponding initial values, a good approximation of the true density in the sense of a backward error analysis. For a more careful and detailed analysis of this type, see [16].

In the applications to fluid dynamics that we have in mind, in [4] equations of motion for the particle positions $\mathbf{q}_i$ and the deformation matrices $\mathbf{H}_i$ are set up describing the interaction of the mass packets with each other. For inviscid flows, they essentially result from a variational principle that is augmented by a frictional term damping the relative motion of the particles to enforce entropy production in shocks. We do not go into details here, but restrict ourselves as in [16] to the much simpler case of the motion in a given external conservative force field

$$\mathbf{f} = -\nabla U \tag{2.21}$$

that can be derived from a continuously differentiable potential $U : \mathbb{R}^d \to \mathbb{R}$. The potential energy of a given mass distribution with mass density ρ is then

$$V(t) = \int U(\mathbf{x})\rho(\mathbf{x},t)\,\mathrm{d}\mathbf{x}, \tag{2.22}$$

and can, for our superposition (2.10) of mass packets, be rewritten as

$$V = \sum_{i=1}^{N} m_i \int U(\mathbf{q}_i+\mathbf{H}_i\mathbf{y})\psi(\mathbf{y})\,\mathrm{d}\mathbf{y}. \tag{2.23}$$

The kinetic energy of the mass packet i is

$$E_i(t) = \frac{1}{2}\int m_i\psi_i(\mathbf{x},t)|\mathbf{v}_i(\mathbf{x},t)|^2\,\mathrm{d}\mathbf{x} \tag{2.24}$$

and attains, because of (2.1) and (2.2), the closed representation

$$E_i = \frac{1}{2}m_i|\mathbf{q}_i'|^2 + \frac{1}{2}Jm_i|\mathbf{H}_i'|^2, \tag{2.25}$$

where $|\cdot|$ denotes the Euclidean norm of a vector and the Frobenius norm of a matrix, respectively. The total kinetic energy of the system is

$$E(t) = \sum_{i=1}^{N} E_i(t). \tag{2.26}$$

From the kinetic energy (2.26) and the internal energy (2.22) the Lagrange function

$$\mathcal{L} = E - V \tag{2.27}$$

of the system is formed, leading to the equations of motion

$$\frac{\mathrm{d}}{\mathrm{d}t}\frac{\partial \mathcal{L}}{\partial \mathbf{q}_i'} - \frac{\partial \mathcal{L}}{\partial \mathbf{q}_i} = \mathbf{0}\,, \quad \frac{\mathrm{d}}{\mathrm{d}t}\frac{\partial \mathcal{L}}{\partial \mathbf{H}_i'} - \frac{\partial \mathcal{L}}{\partial \mathbf{H}_i} = \mathbf{0}. \tag{2.28}$$

Introducing the normalized forces

$$\mathbf{F}_i = -\frac{1}{m_i}\frac{\partial V}{\partial \mathbf{q}_i}\,, \quad \mathbf{M}_i = -\frac{1}{m_i}\frac{\partial V}{\partial \mathbf{H}_i} \tag{2.29}$$

with $\mathbf{f} = -\nabla U$ explicitly given by

$$\mathbf{F}_i = \int \mathbf{f}(\mathbf{q}_i + \mathbf{H}_i\mathbf{y})\psi(\mathbf{y})\,\mathrm{d}\mathbf{y}\,, \quad \mathbf{M}_i = \int [\,\mathbf{f}(\mathbf{q}_i + \mathbf{H}_i\mathbf{y})][\,\mathbf{y}\,]^{\mathrm{T}}\psi(\mathbf{y})\,\mathrm{d}\mathbf{y}, \tag{2.30}$$

these equations read

$$\mathbf{q}_i'' = \mathbf{F}_i\,, \quad \mathbf{H}_i'' = \frac{1}{J}\mathbf{M}_i. \tag{2.31}$$

The masses m_i of the packets cancel, and neither the inverses nor the determinants of the matrices $\mathbf{H}_i$ enter into the final equations of motion. For arbitrary nonconservative force fields $\mathbf{f}$, the equations of motion remain the same.

The calculation of the forces (2.30) requires the computation of integrals living on the reference domain on which the shape function ψ is strictly positive. As described in [4], these integrals are replaced by a quadrature rule

$$\int g(\mathbf{y})\psi(\mathbf{y})\,\mathrm{d}\mathbf{y} \;\to\; \sum_{\nu=1}^{n} \alpha_\nu g(\mathbf{a}_\nu) \tag{2.32}$$

with fixed weights $\alpha_\nu > 0$ and fixed nodes $\mathbf{a}_\nu$ inside the support of the shape function ψ, which plays the role of a weight function here. To maintain the convergence properties of the method, the quadrature formula needs to be exact for second order polynomials [16], where, for sensitive problems, it can be advantageous to increase the degree of exactness further to sample the force density better. We remark that the variational nature of the equations of motion is not affected by this discretization of the integrals (2.30) because one gets the same expressions first discretizing the potential (2.23) and then forming the derivatives. For the shape function ψ the cubic B-spline (2.3), (2.4), a good quadrature rule (2.32) is the tensor product counterpart of the weighted Gaussian formula

$$\int g(\xi)\widetilde{\psi}(\xi)\,\mathrm{d}\xi \;\to\; \frac{5}{27}\,g\Big(-\frac{3}{\sqrt{10}}\Big) + \frac{17}{27}\,g(0) + \frac{5}{27}\,g\Big(\frac{3}{\sqrt{10}}\Big) \tag{2.33}$$

in one space dimension. It has been used in the numerical experiments in section 5 and is even exact for fifth order polynomials.

3. The basic restart procedure. The ability of the mass packets to deform arbitrarily with the flow and to change their size, shape, and orientation is the reason for the high accuracy of the finite mass method, but can also lead to serious problems when particles become sharp needles or degenerate in another way. In such situations, a restart of the computation is necessary in which the mass density, the velocity field, and the other field quantities are represented by a new set of non-deformed particles

$$\bar\psi_\nu(\mathbf{x}) \;=\; \frac{\psi\big(\bar{\mathbf{H}}_\nu^{-1}(\mathbf{x}-\bar{\mathbf{q}}_\nu)\big)}{\det\bar{\mathbf{H}}_\nu} \tag{3.1}$$

with given centers $\bar{\mathbf{q}}_\nu$ and deformations $\bar{\mathbf{H}}_\nu$, where the variable t is suppressed as we are considering a fixed time. In the case finally discussed here, the positions $\bar{\mathbf{q}}_\nu$ are points of an infinitely extended regular grid and the deformation matrices $\bar{\mathbf{H}}_\nu$ the same for all particles. The first step is to decompose the mass densities

$$\psi_i(\mathbf{x}) \;=\; \frac{\psi\big(\mathbf{H}_i^{-1}(\mathbf{x}-\mathbf{q}_i)\big)}{\det\mathbf{H}_i} \tag{3.2}$$

of the old, deformed particles approximately into weighted sums

$$m_i\,\psi_i(\mathbf{x}) \;\to\; \sum_\nu \bar m_{i\nu}\,\bar\psi_\nu(\mathbf{x}) \tag{3.3}$$

of finitely many of the new mass densities (3.1). How the coefficients $\bar m_{i\nu}$ are chosen is of no importance for the moment and will be discussed later. The fragments of the old particles are then recombined to new particles with the mass densities

$$\bar m_\nu\,\bar\psi_\nu(\mathbf{x}), \quad \bar m_\nu \;=\; \sum_i \bar m_{i\nu}, \tag{3.4}$$

that superimpose to the new total mass density

$$\bar\rho(\mathbf{x}) \;=\; \sum_\nu \bar m_\nu\,\bar\psi_\nu(\mathbf{x}). \tag{3.5}$$

Next, the velocity fields (2.12) of the old particles are transferred to the fragments into which they split now, that is, their mass flux densities are decomposed into

$$m_i\,\psi_i(\mathbf{x})\mathbf{v}_i(\mathbf{x}) \;\to\; \sum_\nu \bar m_{i\nu}\,\bar\psi_\nu(\mathbf{x})\mathbf{v}_i(\mathbf{x}). \tag{3.6}$$

In the same fashion as the mass densities, the mass flux densities of the fragments are recombined to the mass flux densities

$$\bar m_\nu\,\bar\psi_\nu(\mathbf{x})\bar{\mathbf{v}}_\nu(\mathbf{x}), \quad \bar{\mathbf{v}}_\nu(\mathbf{x}) \;=\; \sum_i \frac{\bar m_{i\nu}}{\bar m_\nu}\,\mathbf{v}_i(\mathbf{x}), \tag{3.7}$$

of the new particles. Introducing the quantities

$$\bar{\mathbf{q}}'_\nu \;=\; \sum_i \frac{\bar m_{i\nu}}{\bar m_\nu}\,\mathbf{v}_i(\bar{\mathbf{q}}_\nu), \quad \bar{\mathbf{H}}'_\nu\bar{\mathbf{H}}_\nu^{-1} \;=\; \sum_i \frac{\bar m_{i\nu}}{\bar m_\nu}\,\mathbf{H}'_i\mathbf{H}_i^{-1}, \tag{3.8}$$

the velocity fields $\bar{\mathbf{v}}_\nu$ in (3.7) attain the usual representation

$$\bar{\mathbf{v}}_\nu(\mathbf{x}) \;=\; \bar{\mathbf{q}}'_\nu + \bar{\mathbf{H}}'_\nu\bar{\mathbf{H}}_\nu^{-1}(\mathbf{x}-\bar{\mathbf{q}}_\nu) \tag{3.9}$$

with the matrices $\bar{\mathbf{H}}'_\nu = (\bar{\mathbf{H}}'_\nu \bar{\mathbf{H}}_\nu^{-1})\bar{\mathbf{H}}_\nu$ implicitly given by (3.8). The mass flux densities (3.7) of the new particles add up to the new total mass flux density

$$(\bar{\rho}\bar{\mathbf{v}})(\mathbf{x}) \;=\; \sum_\nu \bar{m}_\nu\, \bar{\psi}_\nu(\mathbf{x})\bar{\mathbf{v}}_\nu(\mathbf{x}), \tag{3.10}$$

and so again define the new total velocity field $\bar{\mathbf{v}}$. Provided the coefficients $\bar{m}_{i\nu}$ are all nonnegative, the new particle velocities $\bar{\mathbf{v}}_\nu$ and therefore also the total velocity field $\bar{\mathbf{v}}$ itself are local convex combinations of the velocity fields $\mathbf{v}_i$ of the original particles. Hence in this case it is rather unlikely that oscillations are introduced. The second order accuracy of the velocity approximation is maintained with this construction. Finally, the restart widely eliminates the fluctuation of the particle velocities.

We now turn to the decomposition (3.3) of the original particles i into the new, nondegenerated particles ν. Starting point is a quasi-interpolation operator

$$(Qf)(\mathbf{x}) \;=\; \sum_\nu Q_\nu(f)\, \psi\big(\bar{\mathbf{H}}_\nu^{-1}(\mathbf{x} - \bar{\mathbf{q}}_\nu)\big) \tag{3.11}$$

on a regular grid at least reproducing linear functions, which is essential to preserve the second order accuracy of the method. The Q_ν are linear functionals of the form

$$Q_\nu(f) \;=\; \sum_{k=1}^{n} \alpha_k^{(\nu)} f(\bar{\mathbf{q}}_\nu + \bar{\mathbf{H}}_\nu \mathbf{a}_k) \tag{3.12}$$

with weights $\alpha_k^{(\nu)}$ and nodes $\mathbf{a}_k$ independent of ν. We then approximate the old mass density ρ by its quasi-interpolant $\bar{\rho} = Q\rho$, or more precisely set

$$\bar{m}_{i\nu} \;=\; \det \bar{\mathbf{H}}_\nu\, Q_\nu(m_i\psi_i). \tag{3.13}$$

At most positions, the weights $\alpha_k^{(\nu)}$ are set to fixed values α_k independent of ν, but in critical regions like shockfronts or other points of discontinuity it can be advantageous to switch over to different schemes to stabilize the computation.

Barring all accuracy considerations, a sufficiently large number of sampling points is necessary to smooth the data and to avoid instabilities. It should however be noted that the computation of the quantities (3.13) is a purely local process and that only the values (3.13) themselves are needed to assemble the masses (3.4) and the velocities (3.9) of the new particles. Other scalar quantities like the entropy density [4] are transferred in the same way as the mass density to the new particles.

4. A variant with reduced diffusion. As long as the coefficients $\alpha_k^{(\nu)}$ in (3.12) are all positive, the $\bar{m}_{i\nu}$ cannot attain values less than zero, with the described consequences for the velocities $\bar{\mathbf{v}}_\nu$. Moreover, if $f \le g$, then also $Qf \le Qg$. In particular, if $\alpha \le f \le \beta$ with constant values α and β, $\alpha \le Qf \le \beta$. The disadvantage of such restart procedures, however, is that they introduce a rather strong diffusion, which does not fit well to a Lagrangian approach like the finite mass method. Such effects can be largely avoided by treating the velocity field and the mass density differently.

The mass density should be approximated as well as it is possible with the given functions $\bar{\psi}_\nu$, already to conserve mass sufficiently well during the restart process. This can best be achieved forcing up the polynomial accuracy of the quasi-interpolation operator (3.11) as far as possible. It can happen that particles ν with negative masses first are generated then, the surrounding of which requires a special treatment.

A high polynomial accuracy of the quasi-interpolation operator (3.11) does not, however, improve the quality of the velocity approximation and can in contrast have very negative effects. The reason is that the velocity fields of the single particles must individually well approximate the exact velocity field. Negative coefficients $\alpha_k^{(\nu)}$ could even lead to particles moving into the wrong direction, yielding strange results and a bad approximation of the flow. Therefore, the velocities of the new particles should be computed using an operator (3.11) guaranteeing that $Qf \geq 0$ for functions $f \geq 0$. Its polynomial accuracy does not affect the second order accuracy of the velocity approximation and is only of minor importance in the given context.

In the case of tensor product cubic B-splines $\bar\psi_\nu$ as considered in section 2 on a regular grid of a gridsize h, quasi-interpolation operators of the form (3.11), (3.12) can be built up in an obvious way from the corresponding quasi-interpolation operators

$$(Qf)(\xi) \;=\; \sum_{\nu=-\infty}^{\infty} Q_\nu(f)\,\widetilde\psi\Big(\frac{\xi - h\nu}{h}\Big) \tag{4.1}$$

in one space dimension where

$$Q_\nu(f) \;=\; \sum_{k=-n}^{n-1} \alpha_k^{(\nu)} f(h\nu + ha_k) \tag{4.2}$$

with symmetrically arranged nodes and weights. The resulting quasi-interpolation operator (3.11), (3.12) then reproduces linear polynomials if and only if the condition

$$\sum_{k=-n}^{n-1} \alpha_k^{(\nu)} \;=\; 1 \tag{4.3}$$

is satisfied. It is exact for second- and even third-order polynomials and then fully exploits the order of accuracy attainable with cubic splines if and only if additionally

$$\sum_{k=-n}^{n-1} \alpha_k^{(\nu)} a_k^2 \;=\; -\sum_{l=-\infty}^{\infty} l^2\,\widetilde\psi(l). \tag{4.4}$$

Since the right-hand side of this equation is negative, the second condition can only hold if some of the coefficients α_k are negative. The two missing conditions are automatically satisfied by the symmetry of the configuration. To approximate the mass density and related scalar quantities outside points of discontinuity, we set

$$a_k = \frac{2k+1}{n}, \quad \alpha_k = Aa_k^2 + B, \tag{4.5}$$

and determine A and B so that both conditions are fulfilled, which means that among the admissible α_k those are chosen that minimize the sum over the α_k^2. Near points of discontinuity, one falls back to a modified scheme as will be described below to suppress instabilities. To calculate the new particle velocities, the α_k are set to

$$\alpha_k \;=\; C\,\widetilde\psi(a_k) \tag{4.6}$$

with the a_k the same as above and C chosen such that the normalization condition (4.3) is satisfied. As mentioned, a large number of sampling points is needed to smooth

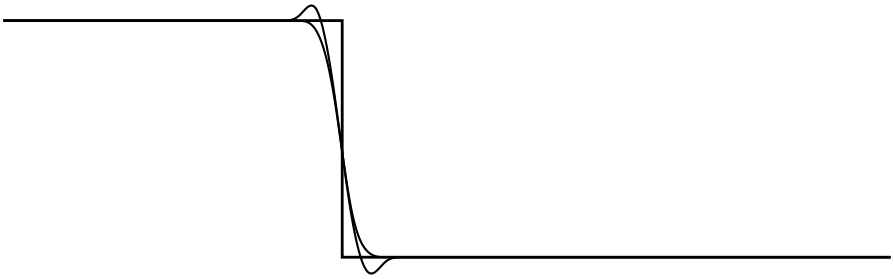

FIG. 1. *The interpolants of a discontinuous function without and with the limiter*

the data sufficiently. In our experiments, we have set $n = 10$. Even values of n are preferable since the old particle densities are then evaluated at the same points for neighboring gridpoints ν and the mass density is then sampled on a uniform grid.

In points of discontinuity, the negative coefficients α_k in the fourth-order scheme based on (4.5) lead to oscillations. To avoid such problems, one can compare the masses $\bar{m}_\nu$ calculated by means of this scheme and the masses m'_ν used in the computation of the new velocities calculated by means of the coefficients (4.6). Because

$$\bar{m}_\nu,\, m'_\nu \;=\; h^d\,(\rho(\bar{\mathbf{q}}_\nu) + \mathcal{O}(h^2)) \tag{4.7}$$

there, they differ only by a value of order $\mathcal{O}(h^{d+2})$ where ρ is smooth, whereas in points of discontinuity like shocks their difference behaves like $\mathcal{O}(h^d)$. If therefore

$$|\bar{m}_\nu - m'_\nu| \;\geq\; \frac{h}{\vartheta}\, h^d \rho_0 \tag{4.8}$$

with $\vartheta > 0$ and $\rho_0 > 0$ user specified constants having the dimension of a length and a density, respectively, the coefficient $\bar{m}_\nu$ then is rejected and replaced by $\bar{m}_\nu = m'_\nu$. Fig. 1 shows the function of this limiter comparing the original and the modified interpolant. Both to circumvent problems with negative particle masses and to prevent an unnecessary spread of particles separating from the boundary, particles ν with masses

$$\bar{m}_\nu \;\leq\; h^d \rho_* \tag{4.9}$$

are ignored, where $\rho_* > 0$ represents a problem dependent lower density bound. The neglected particle densities sum up to a density nowhere exceeding this bound. Because of (4.7), second order accuracy is preserved choosing ρ_* of order h^2. Should the occasion arise, additional criteria are necessary to single out particles in the course of the simulation, for example when they are leaving a certain region.

5. Numerical experiments. The finite mass method has been designed to solve problems in fluid mechanics and in particular to simulate complicated free flows in vacuum in the presence of strong external forces as they occur in astrophysics. The method in combination with a restart procedure similar to this in the previous section has been applied very successfully to such problems [6], [7]. An example of this type will be shortly presented in the next section. To study the behavior of the restart procedure, it is however preferable first to consider simpler test examples. We restrict ourselves in this section to flows in given external force fields because the restart procedure in the end does not recognize where the data are coming from.

For reference, we recall the two equations governing the flow of mass in an external force field with specific force density $\mathbf{f} : \mathbb{R}^d \times \mathbb{R} \to \mathbb{R}^d$, the continuity equation

$$\frac{\partial \rho}{\partial t} + \operatorname{div}(\rho \mathbf{v}) = 0 \tag{5.1}$$

expressing conservation of mass and the momentum equation

$$\frac{\partial \mathbf{v}}{\partial t} + (\nabla \mathbf{v})\mathbf{v} = \mathbf{f} \tag{5.2}$$

for the velocity field $\mathbf{v}$. With $\mathbf{v}$ determined by (5.2) and the initial conditions, the continuity equation (5.1) becomes a linear transport equation for the mass density ρ. Here we are considering two-dimensional motions in conservative force fields

$$\mathbf{f}(\mathbf{x}) = -U'(r)\,\frac{\mathbf{x}}{r}\,, \quad r = |\mathbf{x}|\,, \tag{5.3}$$

with $U'(r) > 0$, that is pointing into the direction of the origin. A stationary velocity field $\mathbf{v}(\mathbf{x}, t) = \mathbf{v}(\mathbf{x})$ solving the momentum equation (5.2) is then

$$\mathbf{v}(\mathbf{x}) = \omega(r)\begin{pmatrix} -x_2 \\ x_1 \end{pmatrix} \tag{5.4}$$

where $\omega(r)$ denotes the angular velocity

$$\omega(r) = \sqrt{\frac{U'(r)}{r}}\,. \tag{5.5}$$

Mass points moving in this velocity field follow the circular trajectories

$$t \;\to\; \mathbf{Q}(\omega(r)t)\,\mathbf{x} \tag{5.6}$$

where $\mathbf{Q}(\varphi)$ denotes the two-dimensional rotation

$$\mathbf{Q}(\varphi) = \begin{pmatrix} \cos\varphi & -\sin\varphi \\ \sin\varphi & \cos\varphi \end{pmatrix}. \tag{5.7}$$

With given mass density ρ_0 at time $t = 0$, the mass density at time t correspondingly is

$$\rho(\mathbf{x}, t) \;=\; \rho_0\big(\mathbf{Q}(\omega(r)t)^{\mathrm{T}}\mathbf{x}\big). \tag{5.8}$$

This looks harmless, but depending on the resulting angular velocity a rather dramatic behavior can be hidden behind these solution formulas. In contrast to fluid dynamics there are no regularizing viscous or pressure forces here!

To trace the motion of a mass distribution in the force field (5.3), we have covered the plane with an infinite rectangular grid of a given gridsize h. The initial positions $\mathbf{q}_i$ of the particles at time $t = 0$ then have been selected from the gridpoints $h\boldsymbol{\nu}$, $\boldsymbol{\nu} \in \mathbb{Z}^2$, and the initial deformation matrices have correspondingly been set to $\mathbf{H}_i = h\,\mathbf{I}$. The active particles and their masses have been determined as described in section 4. Remembering (2.18) and (2.19), the initial velocities of the particles have been set to

$$\mathbf{q}_i' = \mathbf{v}(\mathbf{q}_i), \quad \mathbf{H}_i' = (\nabla \mathbf{v})(\mathbf{q}_i)\,\mathbf{H}_i. \tag{5.9}$$

If not exactly calculable, the motion of the particles has been followed with a high-order, adaptive Runge-Kutta method setting the error tolerance to a value that excludes almost any influence of the time integrator to the total error.

As long as the angular velocity $\omega(r)$ remains constant, that is, for

$$U(r) = \frac{1}{2}\, r^2, \quad \mathbf{f}(\mathbf{x}) = -\mathbf{x}, \tag{5.10}$$

not much happens and the whole configuration simply rotates around the origin. Neither the position of the mass packets relative to each other nor their size or shape changes in this case because the solutions of the equations of motion then read

$$\mathbf{q}_i(t) = \mathbf{Q}(t)\mathbf{q}_i(0), \quad \mathbf{H}_i(t) = \mathbf{Q}(t)\mathbf{H}_i(0). \tag{5.11}$$

The finite mass method works perfectly in this situation. Since the velocity fields of all particles coincide before the first restart with the here linear velocity field

$$\mathbf{v}(\mathbf{x}) = \begin{pmatrix} -x_2 \\ x_1 \end{pmatrix}, \tag{5.12}$$

and since the velocity fields of the new particles are by construction convex combinations of the velocity fields of the old particles, the total velocity field is exactly reproduced here. Therefore examples like this exclusively measure the error due to the restart procedure for the mass density.

We have followed the motion of a rotationally symmetric mass agglomeration of radius 0.1 and center in distance 1 to the origin over ten revolutions. Its internal mass distribution was given by the spline (2.4) with the maximum mass density normalized to 1. The computation was newly set up 61 times after time intervals of equal length, with the last restart after the tenth revolution has been completed. To perform convergence studies, we worked with the three different initial gridsizes

$$h = \frac{L}{1024}, \frac{L}{2048}, \frac{L}{4096}, \tag{5.13}$$

with $L = 2.22$ the sidelength of a square covering the trajectory of the ball and set the corresponding lower density bounds ρ_* in (4.9) to 4×10^{-8}, 10^{-8}, 0.25×10^{-8}. The ratio of the two constants in (4.8) has simply been set to the value $\rho_0/\vartheta = 1$.

The example underlines the importance of the criterion (4.9) to select the particles removed from the computation after a restart. Fig. 2 shows a detail of the configuration arising from the coarsest initial grid after the tenth restart with the particle size for clarity reduced by a corresponding factor. The black particles are those that remain, if one proceeds as described above ignoring particles with masses less than or equal to $h^d\rho_*$ and the other the additionally generated spurious particles when only those with negative masses are taken out of the computation.

To measure how well the mass density is reproduced by the restarts, we have sampled both the exact mass density (5.8) and the approximate mass densities resulting from the superposition of the particles with masses passing the given criteria at the initial time and before and after every restart on a grid five times finer than the finest grid above, and we have computed the corresponding discrete L_2-norms of the mass density itself and of the errors. Fig. 3 shows how these quantities evolve during the given 10 revolutions or 61 restarts, where the errors corresponding to the three gridsizes have been rescaled by the factors 1600, $2^p \times 1600$ and $2^p \times 2^p \times 1600$, respectively, with $p = 3.62$ here. The three error curves almost cover each other, showing that the rate of convergence, not surprisingly, approaches $p = 4$ in this particular example. Mass, angular momentum, and total energy are conserved correspondingly well.

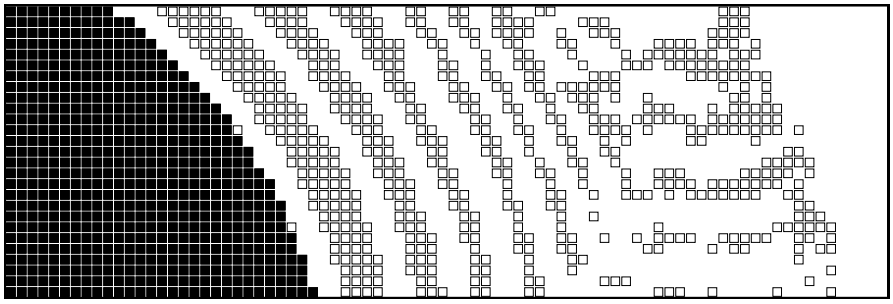

FIG. 2. *The result of different particle selection strategies.*

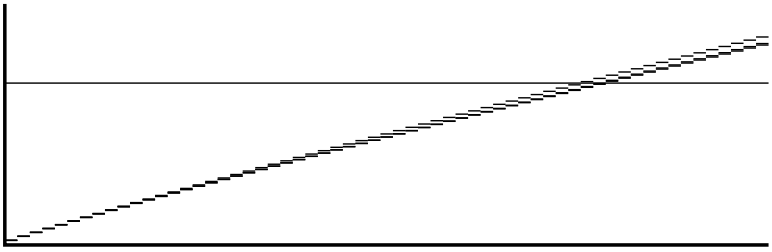

FIG. 3. *The evolution of the mass density and the rescaled errors for the rotating bump.*

The example demonstrates that, despite the fact that the old and the new particles are not aligned with each other, the scheme is able to exploit the high order of accuracy of the given quasi-interpolation operator for the mass density and lets expect that the errors introduced by the restart procedure are comparatively small in most cases.

A much harder challenge than such rotations form Kepler motions in the potential

$$U(r) = -\frac{1}{r} \tag{5.14}$$

arising from the gravitational attraction of a point mass located at the origin. Examples of this type can serve to test the usefulness of our restart procedure for applications in astrophysics like the formation of accretion disks. The angular velocity

$$\omega(r) = \frac{1}{r^{3/2}} \tag{5.15}$$

here induces a very strong shear in tangential direction. The deformation matrices rapidly deteriorate so that the flow cannot be followed without frequent restarts.

It is surprising how well the finite mass method masters this situation and how well it reproduces a dust ring with internal mass distribution again given by the spline (2.4) and maximum density normalized to 1 extending over the region $0.9 \le r \le 1.1$ over many revolutions. To estimate the speed of convergence, we worked with particles initially and after every restart located on grids with gridsizes twice as big as in the previous example and correspondingly quadrupled lower density bounds. The computation was newly set up every time when a mass point on a circular trajectory of radius 1 has covered an angle of 60°. Fig. 4 shows how the particles look after and before a restart, where for clarity they have again been shrunk by some factor.

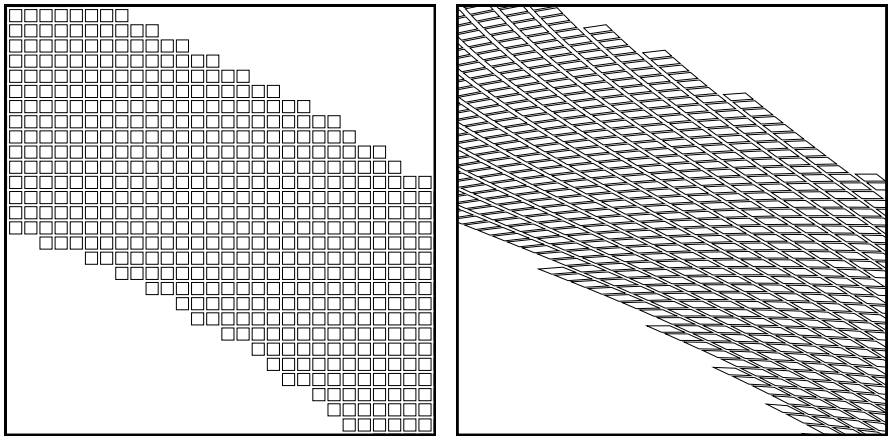

FIG. 4. *The particles in the Kepler motion after and before a restart.*

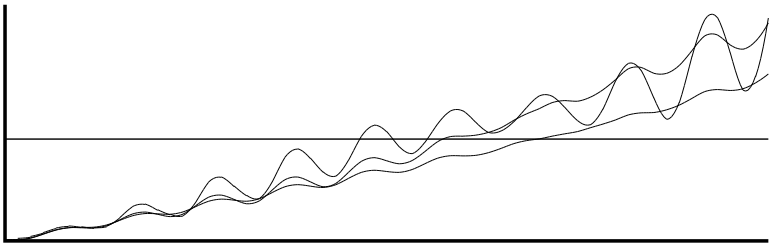

FIG. 5. *The evolution of the mass density and the rescaled errors for the Kepler motion.*

The errors have been measured in the same way as in the preceding example. Fig. 5 shows how the mass density and the corresponding errors evolve during the first ten revolutions here related to the radius 1, where the errors associated with the different grids here have been rescaled by the factors 100, 4×100 and 16×100, respectively. The results for the mass flux density look similar. The error roughly decreases by the factor four when halving the gridsize which confirms the second order accuracy of the finite mass method. The error in the mass flux density almost completely originates from the error in the mass density; the velocity field where is defined is much better approximated than the mass density or the mass flux density, which underpins the strategy developed in section 3. The most important observation in the given context, however, is that the errors introduced by the restarts are orders of magnitude less than the errors introduced by the method itself in between. They exist, but are so small that one cannot recognize them in the picture.

For the middle of the three discretizations, the difference between the exact and the calculated density profile is in the order of less than one percent after the ten revolutions. Fig. 6 shows a cross section of the mass density along a part of the positive x_1-axis at the end of the computation together with the error magnified by the factor 100. The picture corresponds to a one-dimensional initial resolution of less than 100 particles on the interval $0.9 \leq x_1 \leq 1.1$ on which the exact mass density differs from zero; on the diagonal $x_1 = x_2$ the resolution reduces to approximately 65 particles. The mass slowly drifts outwards, which probably represents the main reason for

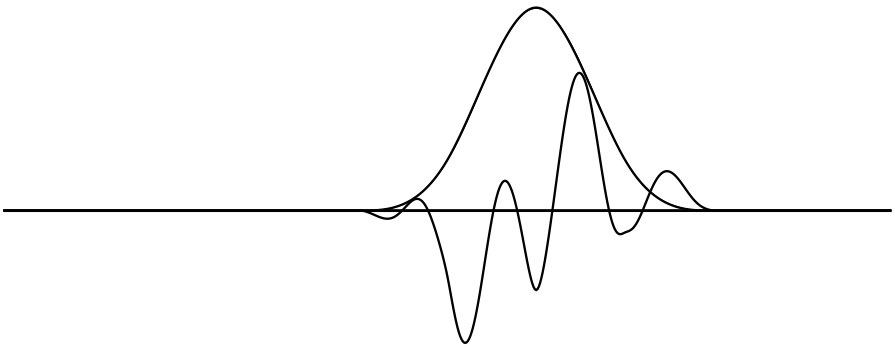

FIG. 6. *A cross section of the mass density and the error* $\times 100$ *after ten revolutions.*

the observed increase of the error, and is typical for such problems. The qualitative behavior however is nearly perfect. The total mass, the angular momentum, and the total energy remain constant up to an error that, though slightly increasing in time, is at the end of the computation for particles of the given initial size still four orders of magnitude less than the considered quantities themselves. This is due to the fact that mass, angular momentum, and total energy are exactly conserved between the restarts (compare [4]), provided the equations of motion are exactly solved, of course, and again reflects the high accuracy of the restart procedure. For the total mass one observes fourth order convergence!

6. An example from astrophysics. Astrophysical flows are characterized by the presence of often dominating external forces like gravitation or of electromagnetic nature, by strong thermodynamical effects including radiation, and by nonlocal self-interactions requiring the solution of additional partial differential equations, for example for the gravitational or the magnetic field. The velocity, the mass density, the pressure, and the temperature usually range over many orders of magnitude, from near vacuum to states never reached on earth. Flows of this kind form a challenge for every numerical method. The finite mass method has originally been designed to complement the in such fields of application very popular smoothed particle hydrodynamics [11], [2] by a more accurate and mathematically better underpinned gridless discretization scheme. It was successfully applied to problems of this type [6], [7]. The aim of this section is to give an impression of such computations and to demonstrate that the finite mass method meanwhile represents a serious tool in application areas like this. Restarts are inevitable in such computations because the strong and very inhomogeneous forces acting upon the particles let them quickly deteriorate.

The system we are considering here is a thin accretion disk circulating around one of the stars in a double star system consisting of two stars with masses m_0 and m_1 that move under reciprocal gravitational attraction on the circular trajectories

$$\mathbf{x}_0(t) \;=\; -\,\frac{m_1}{m_0+m_1}\,\mathbf{Q}(\omega t)\mathbf{e}, \quad \mathbf{x}_1(t) \;=\; \frac{m_0}{m_0+m_1}\,\mathbf{Q}(\omega t)\mathbf{e} \tag{6.1}$$

around the origin, their joint center of mass. The vector $\mathbf{e}$ fixes the distance of the stars to each other and is connected with the angular velocity ω by the relation

$$\omega^2 \;=\; \frac{m_0+m_1}{r^3}, \quad r = |\mathbf{e}|. \tag{6.2}$$

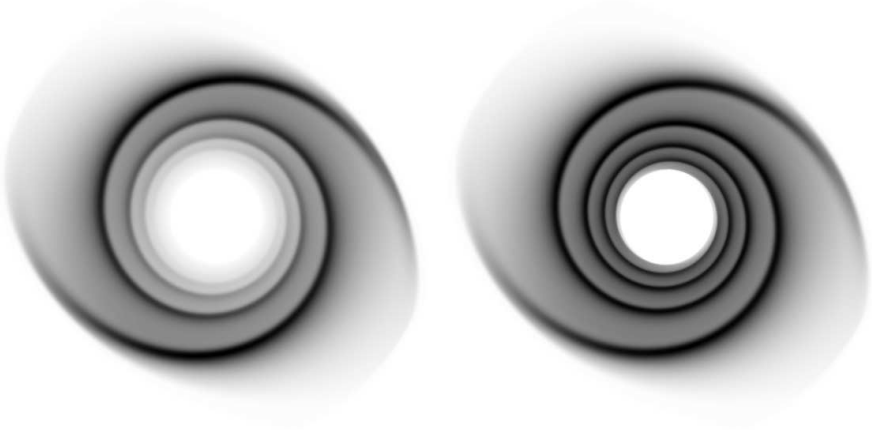

FIG. 7. *The evolution of the mass density in the double star system.*

The dynamics of the disk in the corresponding time-dependent gravitational field

$$\mathbf{f} \;=\; -\,\nabla U, \quad U \;=\; -\,\frac{m_0}{|\,\mathbf{x}-\mathbf{x}_0|} \;-\; \frac{m_1}{|\,\mathbf{x}-\mathbf{x}_1|} \tag{6.3}$$

of the stars is described by the continuity equation (2.17), the momentum equation

$$\rho\left\{\frac{\partial \mathbf{v}}{\partial t} + (\nabla \mathbf{v})\mathbf{v}\right\} = -\nabla\pi + \rho\,\mathbf{f} \tag{6.4}$$

now complemented by the internal pressure force $-\nabla\pi$, and by the equation

$$\frac{\partial s}{\partial t} + \operatorname{div}(s\mathbf{v}) = 0 \tag{6.5}$$

for the entropy density s, stating that the motion stays adiabatic and at the same time guaranteeing conservation of energy. By the laws of thermodynamics, the pressure

$$\pi \;=\; \frac{\partial \varepsilon}{\partial \rho}\rho + \frac{\partial \varepsilon}{\partial s}s - \varepsilon \tag{6.6}$$

can be expressed in terms of the internal energy ε that is again a function of the mass density ρ and the entropy density s. The finite mass method makes the ansatz

$$s(\mathbf{x},t) \;=\; \sum_{i=1}^{N} S_i(t) m_i\, \psi_i(\mathbf{x},t) \tag{6.7}$$

for the entropy density that, for the specific entropies S_i of the particles kept constant, automatically ensures the conservation of entropy (6.5). It treats the pressure forces acting upon the particles as potential forces derived from the internal energy

$$V \;=\; \int \varepsilon(\rho, s)\, \mathrm{d}\mathbf{x} \tag{6.8}$$

considered as a function of the particle positions $\mathbf{q}_i$ and the deformation matrices $\mathbf{H}_i$. To stabilize the computation and to enable shock calculations, proper frictional forces

between the particles must be added partially converting the fluctuation energy between the particles to heat. For details, we refer to [4], and concerning the simulation of accretion disks to the thesis [6] of Klingler and to [7].

The result of such a computation represented in a rotating coordinate system in which the position of both stars remains fixed is shown in Fig. 7. The binary system considered there is characterized by the data $m_0+m_1=1$, $m_0/m_1=0.15$ and $r=1$. The internal energy ε is that of an ideal gas with the ratio $\gamma=5/3$ of the specific heats. The initial data were chosen similar as in the second example of the previous section with the gas ring initially centered around the heavier of the two stars and nearly filling its Roche lobe, the domain on which its gravitational attraction dominates the gravitational attraction of its counterpart. Particles coming too close to the central star were removed from the computation. The flow is extremely violent. Near this inner boundary of the disk, its Mach number reaches the value $M=25$, which means that its velocity exceeds the speed of sound by this factor there! One recognizes that a complicated spiral structure forms that turned out to be rather stable.

Of course, the exact solution of problems like this is unknown, so that it is not easy to judge the quality of such solutions. The results have been verified with advanced grid methods, and it can surely be stated that the finite mass method favorably compares both with such methods and with the smoothed particle hydrodynamics.

REFERENCES

[1] T. Chan, J. Shen, L. Vese, *Variational PDE models in image processing*, Notices Amer. Math. Soc., 50 (2003), pp. 14-26.

[2] O. Flebbe, S. Münzel, H. Herold, H. Riffert, H. Ruder, *Smoothed particle hydrodynamics: physical viscosity and the simulation of accretion disks*, Astrophys. J. , 431 (1994), pp. 754–760.

[3] Chr. Gauger, *Erweiterungen der Methode der Finiten Massen*, Dissertation, Universität Tübingen, Tübingen 2000.

[4] Chr. Gauger, P. Leinen and H. Yserentant, *The finite mass method*, SIAM J. Numer. Anal., 37 (2000), pp. 1768–1799.

[5] M. Griebel and M.A. Schweitzer (eds.), *Meshfree Methods for Partial Differential Equations*, Lect. Notes Comput. Sci. Eng. 26, Springer, Heidelberg 2002.

[6] M. Klingler, *Die Methode der Finiten Massen in der astrophysikalischen Hydrodynamik*, Dissertation, Universität Tübingen, Tübingen 2003.

[7] M. Klingler, *Hydrodynamic simulations of the accretion disk in U Geminorum. The occurence of a two armed spiral structure during outburst*, SFB 382 Report Nr. 190, Universität Tübingen, Tübingen 2003.

[8] M. Klingler, P. Leinen and H. Yserentant, *The finite mass method on domains with boundary*, SIAM J. Sci. Comput., 26 (2005), pp. 1744–1759.

[9] D. Kröner, *Numerical Schemes for Conservation Laws*, Teubner, Stuttgart 1997.

[10] R.J. LeVeque, *Numerical Methods for Conservation Laws*, Birkhäuser, Basel 1990.

[11] J.J. Monaghan, *Smoothed particle hydrodynamics*, Ann. Rev. Astron. Astrophys., 30 (1992), pp. 543–574.

[12] J. Weikert, *Anisotropic Diffusion in Image Processing*, Teubner, Stuttgart 1998.

[13] H. Yserentant, *A particle model of compressible fluids*, Numer. Math., 76 (1997), pp. 111–142.

[14] H. Yserentant, *Particles of variable size*, Numer. Math., 82 (1999), pp. 143–159.

[15] H. Yserentant, *Entropy generation and shock resolution in the particle model of compressible fluids*, Numer. Math., 82 (1999), pp. 161–177.

[16] H. Yserentant, *The convergence of the finite mass method for flows in given force and velocity fields*, in [5], pp. 419–440.